Coarse graining DEM simulations of a powder die-filling system

Putri Mustika Widartiningsih[a], Yuki Mori [a], Kazuya Takabatake [a], Chuan-Yu Wu [b], Kensuke Yokoi[c], Akira Yamaguchi [d], Mikio Sakai[e,*]

[a] Department of Nuclear Engineering and Management, School of Engineering, The University of Tokyo, 7-3-1 Hongo, Bunkyo-ku, Tokyo 113-8656, Japan

[b] Department of Chemical and Process Engineering, University of Surrey, Guildford, Surrey GU2 7XH, United Kingdom

[c] School of Engineering, Cardiff University, Cardiff CF24 3AA, United Kingdom

[d] Nuclear Professional School, School of Engineering, The University of Tokyo, 2-22 Shirakata, Tokai-mura, Naka-gun, Ibaraki 319-1188, Japan

[e] Resilience Engineering Research Center, School of Engineering, The University of Tokyo, 7-3-1 Hongo, Bunkyo-ku, Tokyo 113-8656, Japan

Corresponding author:

Mikio Sakai

mikio_sakai@n.t.u-tokyo.ac.jp

TEL +81-3-5841-6977

FAX +81-3-5841-6981

Abstract

Application of numerical simulations are desired to improve the quality of powder products and to optimize the production process in powder die-filling. In the powder die-filling, complex gas-solid interaction should be simulated since solid particles are significantly influenced by gas flow under moving wall boundary. The discrete element method (DEM) coupled with computational fluid dynamics (CFD) has been widely utilized in the simulation of gas-solid flows, and the adequacy has been proved through countless studies. On the other hand, the existing DEM-CFD method is extremely difficult to simulate the gas-solid flow where the wall boundary is moving. Besides, in the existing DEM-CFD method, huge number of computational particles cannot be simulated on a single PC. Hence, numerical simulations of the industrial powder die-filling becomes a challenging topic from a viewpoint of evolution of the DEM-CFD method, because modeling of the moving wall boundary as well as modeling of large number of computational particles should be considered simultaneously. Very recently, the authors' group has developed the Integrated DEM-CFD method including the arbitrary shape wall boundary model and the scaling law model. In the Integrated DEM-CFD method, the wall boundary is modeled by the signed distance functions and the immersed boundary method, and besides the coarse graining DEM is employed as the scaling law model. Adequacy of the Integrated DEM-CFD method has been proved through verification tests. In the current study, applicability of the Integrated DEM-CFD method is examined in the powder die-filling. Adequacy of the Integrated DEM-CFD method is shown by agreement between the original particle system and the coarse graining particle system in the powder die-filling. Through the verification tests, macroscopic characteristics of the powder die-filling are shown to be in good agreement between the original

system and the coarse grain model system. Consequently, the Integrated DEM-CFD method is illustrated to be effective for the simulation of the industrial powder die-filling systems.

Keywords: coarse graining DEM, DEM-CFD method, powder die-filling, immersed boundary method, signed distance functions

1. Introduction

Powder die-filling is one of important processes and is extensively involved in various manufacturing industries, in order to create high value components. The die filling process consists of the delivery of a certain amount of powder from a moving feed shoe into a stationary die. The study of the powder die-filling has attracted growing attention from many researchers in recent years as it is considered as a critical stage in controlling the properties of the compacted powder. In particular, the shoe velocity [1], the air presence [2–6], the powder properties [7–9] and the die shapes [8,10] may influence the weight distribution of the deposited powder before the compaction. Understanding the contribution of the operating parameters on the resulting powder mass distribution is essential to control the quality of products. This can be achieved by performing sensitivity analyses for those parameters. However, it may require a huge number of experimental conditions, which is time-consuming and practically expensive. To make the evaluation performed effectively and efficiently, transferring the experimental condition into a versatile numerical simulation is desirable.

To perform the numerical simulation of the die filling, there are some important components need to be considered including modeling of the particles, gas phase, moving wall boundary and interactions between them. The interaction between the solid particles and the gas is modeled by the discrete element method (DEM) coupled with computational fluid dynamics (CFD) [11]. The DEM-CFD method has been extensively used to investigate the solid-fluid interaction problems in various engineering fields such as die filling [2–4], fluidized bed [12,13] and granular transportation systems [14,15]. The applicability of the DEM-CFD method becomes wider since the signed distance functions (SDF) [16] and the immersed boundary method (IBM) [17–21] are introduced for modeling the wall boundaries. The SDF and IBM are developed to express the

wall boundary for the DEM and CFD by the scalar fields. Actually, the SDF/IBM makes it possible to simulate gas-solid flows in arbitrary shape domain. The integration between the DEM-CFD method with the SDF/IBM is referred to as the Advanced DEM-CFD method. Adequacy of the Advanced DEM-CFD method has been verified in a die filling system [6], where the simulation results were well agreed with experimental observation.

Despite the progress has been made to date, performing the Advanced DEM-CFD simulation for an industrial scale die filling system remains an arduous task. In typical industrial processes, the number of computational particles may exceed the maximum limit that can be simulated by the DEM on a single PC. Competition between the required number of calculated particles with the limit of computer capacities remains a key issue. Therefore, further development of DEM-CFD method is necessary. Very recently, the authors' group has originally developed the Integrated DEM-CFD method [22], where the coarse graining DEM is introduced into the Advanced DEM-CFD to make the simulation of large scale gas-solid flow system affordable. In the coarse graining DEM, a large number of original particles are replaced into a small number of parcels, which are referred to as coarse-grained particles. The features of the coarse-grained particle are carefully determined to agree the total energy between the original particle system and the coarse grain model system. When the particle tracking is simulated by the coarse-grained particles, number of calculated particles can be significantly reduced than actual one. Consequently, the huge number of particles in the industrial powder die-filling system can be simulated efficiently by introducing the coarse graining DEM. The coarse graining DEM has been applied to dense granular flow systems in the previous studies such as bubbling fluidized bed [23,24], pneumatic conveying system [25], spouted bed [26] and sedimentation of solids

5

[27]. Verification and validation tests for the Integrated DEM-CFD method have been previously demonstrated [22], where the results are in excellent agreement with experimental observation.

Although numerical simulation of industrial die filling system is highly demanded, it has hardly been performed so far. This is because modeling of moving wall boundary for a gas-solid flow is difficult and because quite a number of particles are required. In order to perform a simulation of the industrial powder die-filling, the Integrated DEM-CFD method is employed in this study. Through this study, adequacy of the Integrated DEM-CFD method is proved by agreement of the macroscopic characteristics between the original particle system and the coarse graining particle system in the powder die-filling. The macroscopic characteristics of the original particle system such as the solid particle spatial location, the air pressure drop, and the filling rates of particles, are illustrated to be reproduced by the integrated DEM-CFD method. Thus, the industrial powder die-filling system is shown to be simulated by the integrated DEM-CFD method.

2. Numerical modeling

2.1. Modeling of the solid phase

The solid particle is modeled by the DEM [28], where the coarse graining DEM is taken into consideration. The idea of the coarse graining DEM is to replace a number of particles with the same properties such as density and mass into a parcel, which is referred to as a coarse-grained particle. The evaluation of the coarse-grained particle is addressed to agree the total energy between the original particle system and the coarse grain model system.

The translational and rotational motions of the coarse-grained particle are governed by Newton's second laws on motions, which are given as

$$m_{CGM}\dot{v}_{CGM} = \sum F_{C_{CGM}} - V_{CGM}\nabla p + F_{D_{CGM}} + F_{g_{CGM}} \tag{1}$$

and

$$I_{CGM}\dot{\omega}_{CGM} = \sum T_{CGM}, \tag{2}$$

where m, v, F_C, V, p, F_D, F_g, I, ω and T represent the mass of the particle, the translational velocity of the particle, the contact force, the particle volume, the pressure, the drag force, the gravitational force, the moment of inertia, the angular velocity of the particle and the torque. The subscript CGM indicates the coarse grain model system.

The representation of the original particles due to the coarse-grained particles is parameterized by the scaling coefficient l, which is referred to as the coarse grain ratio. The relationships between the original system and the coarse grain model system are given as follows

$$d_{CGM} = l d_O, \tag{3}$$

$$m_{CGM} = l^3 m_O, \tag{4}$$

$$I_{CGM} = l^5 I_O, \tag{5}$$

where d is the particle diameter. The subscript O denotes the original particles. The properties of the coarse-grained particles are carefully determined to make mass, momentum, and energy agree between the original particle system and the coarse grain model system.

All the forces acting on the coarse-grained particle is calculated based on the energy agreement between the coarse grained particle and the group of the original particles. All of the

7

original particle are assumed to have equal displacement, translational velocity and rotational velocity in the coarse-grained particle. Besides, when binary collision occurs between the coarse grained particles, l^3 pairs of binary collision assumes to occur simultaneously. The displacement and the velocity of a coarse-grained particle are then modeled to equal with the average of those of the original particles. To satisfy this condition, normal and tangential component of the contact force acting on the coarse-grained particle are expressed by

$$F_{C_{n_{CGM}}} = l^3\left(-k\boldsymbol{\delta}_{n_{CGM}} - \eta\boldsymbol{v}_{n_{CGM}}\right) \tag{6}$$

and

$$F_{C_{t_{CGM}}} = \begin{cases} l^3\left(-k\boldsymbol{\delta}_{t_{CGM}} - \eta\boldsymbol{v}_{t_{CGM}}\right) & \left(\left|F_{C_{t_{CGM}}}\right| < \mu\left|F_{C_{n_{CGM}}}\right|\right) \\ -l^3\mu\left|F_{C_{n_{CGM}}}\right|\boldsymbol{v}_{t_{CGM}}/|\boldsymbol{v}_{t_{CGM}}| & \left(\left|F_{C_{t_{CGM}}}\right| \geq \mu\left|F_{C_{n_{CGM}}}\right|\right) \end{cases} \tag{7}$$

where k, $\boldsymbol{\delta}$, η and μ are the stiffness coefficient, the overlap between the contacting particles, the damping coefficient and the coefficient of friction, respectively. Subscript n and t denote the normal and the tangential component, respectively.

The drag force acting on the coarse-grained particles is given by

$$F_{D_{CGM}} = V_{CGM}\frac{\beta}{1-\varepsilon}\left(\boldsymbol{u}_f - \boldsymbol{v}_{CGM}\right), \tag{8}$$

where β, ε and $\boldsymbol{u}_f$ are the interphase momentum transfer coefficient, the void fraction and the fluid velocity. The value of β is evaluated according to the particle concentration in a grid. The equation by Ergun [29] is used for the dense regimes ($\varepsilon \leq 0.8$), and the Wen & Yu model [30] is applied for the dilute regimes ($\varepsilon > 0.8$), which are written as follows

$$\beta = \begin{cases} 150\dfrac{\mu_f(1-\varepsilon)^2}{\varepsilon d_O^2} + \dfrac{1.75(1-\varepsilon)\rho_f}{d_O}|\boldsymbol{v}_{CGM} - \boldsymbol{u}_f| & (\varepsilon \leq 0.8) \\ \dfrac{3}{4}C_D\dfrac{\varepsilon(1-\varepsilon)\rho_f}{d_O}|\boldsymbol{v}_{CGM} - \boldsymbol{u}_f|\varepsilon^{-2.65} & (\varepsilon > 0.8) \end{cases}. \tag{9}$$

The drag coefficient C_D is expressed as

$$C_D = \begin{cases} \dfrac{24}{Re_p}(1 + 0.15Re_p^{0.687}) & Re_p \leq 1000 \\ 0.44 & Re_p > 1000 \end{cases}, \tag{10}$$

with

$$Re_p = \frac{\varepsilon\rho_f d_O}{\mu_f}|\boldsymbol{v}_{CGM} - \boldsymbol{u}_f|, \tag{11}$$

where Re_p is the particle Reynolds number, μ_f is the dynamic fluid viscosity, and ρ_f is the fluid density.

2.2. Modeling of fluid phase

The motion of the fluid is calculated from the continuity and Navier-Stokes equations where the local volume average technique is considered [31],

$$\frac{\partial\varepsilon}{\partial t} + \nabla \cdot (\varepsilon\boldsymbol{u}_f) = 0 \tag{12}$$

and

$$\frac{\partial}{\partial t}(\varepsilon\rho_f\boldsymbol{u}_f) + \nabla \cdot (\varepsilon\rho_f\boldsymbol{u}_f\boldsymbol{u}_f) = -\varepsilon\nabla p - \boldsymbol{f} + \nabla \cdot (\varepsilon\boldsymbol{\tau}_f) + \varepsilon\rho_f\boldsymbol{g}, \tag{13}$$

where $\boldsymbol{\tau}_f$ is the viscous stress tensor, $\boldsymbol{g}$ is the gravitational acceleration and $\boldsymbol{f}$ is the fluid-particle interaction force per unit volume. The value of $\boldsymbol{f}$ is calculated by summing up the fluid-particle interaction force given in Eq. (8) and divided by the volume of the volume of the CFD grid as

$$\boldsymbol{f} = \frac{\sum_{i=1}^{N_{grid}} \boldsymbol{F}_{D_{CGM}}}{V_{grid}},$$

(14)

where N_{grid} is the number of particles in the CFD grid and V_{grid} is volume of the CFD grid. The two-way coupling between solid and fluid can be achieved by Eq. (14).

2.3. Modeling of wall boundaries

Modeling of the moving and geometrically complex wall boundaries is often required for simulations of industrial systems. Furthermore, the particle-wall and fluid-wall interactions need to be calculated simultaneously. The Integrated DEM-CFD offers an efficient method to model the moving and geometrically complex wall boundaries by introducing the SDF and the IBM. The SDF is applied to model the particle-wall interaction, and the IBM is used to model the fluid-wall interactions. The versatility of the SDF/IBM for modeling the wall boundary in DEM-CFD simulations has been verified in our previous studies [6,22].

The SDF [16,32–36] creates the boundary for the DEM calculations. The wall boundary in SDF $\phi_{SDF}(\boldsymbol{x})$ is expressed in a scalar field, which is formulated as

$$\phi_{SDF}(\boldsymbol{x}) = d(\boldsymbol{x})s(\boldsymbol{x}),$$

(15)

where $d(\boldsymbol{x})$ is the distance between the particle and the wall surface and $s(\boldsymbol{x})$ is the sign of the position. The value of $s(\boldsymbol{x})$ is positive when the particle position is inside the calculational

region, and vice versa. When the particle interacts with the wall, the contact force is calculated based on the closest distance between the particle and the wall surface. The overlap between a solid particle and wall surface $\boldsymbol{\delta}_{PW}$ is written as

$$\boldsymbol{\delta}_{PW} = \left(\phi - \frac{d_{CGM}}{2}\right)\frac{\nabla\phi_{SDF}}{|\nabla\phi_{SDF}|}, \tag{16}$$

where the subscript PW indicates the particle-wall interaction. Thus, the normal component of the particle-wall contact force is expressed as

$$\boldsymbol{F}_{C_{n_{CGM}}} = l^3\left(-k\boldsymbol{\delta}_{PW}|\nabla\phi_{SDF}| - \eta\boldsymbol{v}_{n_{CGM}}\right). \tag{17}$$

Incidentally, the tangential component of the particle-wall contact force is calculated in the same way as Eq. (7).

The IBM [19–21,37] with direct forcing approach is employed to model the wall boundary by introducing a body force into the fluid dynamic. The interaction between the wall boundary object and the fluid is analyzed by the volume-weighted average velocity $\boldsymbol{u}$ [38] as

$$\boldsymbol{u} = (1 - \alpha)\boldsymbol{u}_f + \alpha\boldsymbol{U}_B, \tag{18}$$

where $\boldsymbol{U}_B$ is the local velocity of the wall and α expresses the local volume fraction occupied by the wall. When a grid is judged to be inside of the wall boundary object, α becomes 1 and hence the velocity field is equal to the wall velocity ($\boldsymbol{u} = \boldsymbol{U}_B$). When fluid occupied the grid, the α becomes 0 and hence $\boldsymbol{u} = \boldsymbol{u}_f$. Since the IBM is introduced, the fluid field velocity is considered in the calculation of the fluid dynamics. Thus, when the IBM is used, the Navier-Stokes equation is rearranged as

$$\frac{\partial(\varepsilon\rho_f\boldsymbol{u})}{\partial t} + \nabla \cdot (\varepsilon\rho_f\boldsymbol{uu}) = -\varepsilon\nabla p - \boldsymbol{f} + \nabla \cdot (\varepsilon\boldsymbol{\tau}_f) + \varepsilon\rho_f\boldsymbol{g} + \boldsymbol{f}_{IB}, \tag{19}$$

where $\boldsymbol{f}_{IB}$ is the external forcing on fluid due to the IBM. This external force is formulated as

$$\boldsymbol{f}_{IB} = \frac{\varepsilon\rho_f\alpha(\boldsymbol{U}_B - \hat{\boldsymbol{u}})}{\Delta t}, \tag{20}$$

where $\hat{\boldsymbol{u}}$ represents the temporal velocity field before being modified by the IBM.

3. Simulation conditions

The geometry of the die filling system is illustrated in Fig. 1. The system was composed of a shoe, a table and a die. The calculational domain was 84 mm, 42 mm and 30 mm in x, y and z directions. The calculational domain was discretized by uniform grids with a side length of 0.6 mm. The shoe comprised a cuboid cavity with dimensions of 10 mm, 30 mm and 10 mm in x, y and z directions. The die was a step structure, where deep and shallow section depths were 12 mm and 7 mm, respectively. In the current study, two types of die were considered by positioning the deep section on either the left side or right side of the die. Die type-1 positioned the deep section on the right side, whereas die type-2 was the opposite. Three measurement cells were set inside the die to analyze the fluid pressure drop, namely, cell A, cell B and cell C. The filling process was driven by the translation of the shoe at a velocity of 0.1 m/s.

Table 1 lists the physical properties of the solid and the gas phases. The particle density, the spring constant, the coefficient of friction and the coefficient of restitution were set to be 1,500 kg/m^3, 50 N/m, 0.3 and 0.9, respectively. The fluid was the air with the density of 1.0 kg/m^3 and the viscosity of 1.8×10^{-5} Pa s.

Table 2 summarizes the calculation conditions. Eight simulations had been performed, in which the cases were grouped according to the die type. Each case group employed four types of particle systems, namely, the original particles, the coarse-grained particles with coarse grain ratio being 2.0 and 3.0, and the simply large particles. Case 1 was performed to examine the coarse grain model in die type-1. Case 1-1 employed 540,000 original particles with a diameter of 0.125 mm. Case 1-2 and Case 1-3 employed the coarse-grained particles with a coarse grain ratio of 2.0 and 3.0, respectively. Thus, the calculated particle size in Cases 1-2 and 1-3 became 0.250 mm and 0.375 mm, respectively. The total mass and total volume of the calculation systems were equivalent in Case 1-1, Case 1-2 and Case 1-3. To evaluate the effectiveness of the coarse grain model, Case 1-4 was carried out with simply large-sized particle system. Case 1-4 was performed to examine the effectiveness of the coarse graining DEM, and comparing the calculation results between Case 1-3 and Case 1-4. In Case 1-3 and Case 1-4, diameter of the computational particle was equivalent, where the coarse graining DEM was used in Case 1-3 and was not used in Case 1-4. Simulations of Case 2 were performed in the same manner as Case 1. The evaluation of coarse grain model in die type-2 was carried out in Case 2. Original particles with a number of 540,000 were assigned in Case 2-1. The coarse-grained particles with coarse grain ratio of 2.0 and 3.0 were respectively employed in Case 2-2 and Case 2-3. The effectiveness of the coarse grain model was investigated by employing the simply large particles in Case 2-4, in which the calculated particle size was the same as in Case 2-3. For the initial condition in each simulation, the particles were generated randomly inside the shoe cavity. In order to make a fair comparison between the original particle system and the coarse graining particle systems, the CFD grid size was set equivalently in all the cases. As a matter of course, the CFD grid size should be sufficiently larger than the diameter of the calculated particle due to

the local volume average technique. Besides, spatial resolution of the solid phase should be taken into consideration, when the coarse graining DEM was used in the calculations.

The time step for particle motion was set to 1.0×10^{-6} s. The boundary for solid particles and fluid was modeled by the SDF and IBM, respectively. Fig. 2 shows the vertical cross-section of SDF and IBM of the die filling system with die type-1. As shown in Fig. 2a, the SDF was defined by scalar field including sign and distance. In the SDF, cut-off distance was usually set because of the efficiency. In this study, the cut-off distance was given by 0.001 m. In Fig. 2b, the IBM created the boundary by presenting the local volume fraction of the fluid.

4. Results and discussion

4.1. Case 1

Fig. 3 presents the typical snapshots of particle spatial location and the air flow vector at the die region in Case 1. Those were taken at 0.10 s, 0.15 s, 0.19 s and final state. At first, the particle spatial location in the original particle system (Case 1-1) was described. When the shoe cavity moved over the die inlet, the particles moved into the die from the left side. At 0.10 s, the front of particle stream hit the base of the shallow section of the die. A concave structure was formed on the left side of the particle flow. At 0.15 s, when the shoe cavity aligned with the die inlet, the particle flow narrowed toward the middle region and created void spaces on the left and right sides. The flow hit the edge of the step before cascading over the deep region. As the shoe moved further, the particles fed the deep section at 0.19 s. Finally, the particles were settled inside the die after the shoe passed the die. The resulting pile surface sloped up from the left side to the right side. To investigate the applicability of the coarse graining DEM, the results with the

14

coarse grain ratio of 2.0 (Case 1-2) and 3.0 (Case 1-3) were compared to the original particle system. In Case 1-2 and Case 1-3, the particle flow pattern during the filling stage was quite similar to that in Case 1-1. In particular, the particle spatial location in Case 1-1 were suitably reproduced by Case 1-2 and Case 1-3. The coarse graining DEM could simulate local behavior of the particles such as the impact velocity because the coarse graining DEM could predict the spatial location of the particles observed at 0.10 s. It was demonstrated that the flow of original particles could be reproduced by using the coarse graining DEM in the powder die-filling. The good agreement on the particle behavior between the original particle system and the coarse grain model system was shown not only at the final state but also during the filling process. To show the effectiveness of the coarse graining DEM, Case 1-4 was simulated without the coarse graining DEM (simply large particle system), where diameter of the computational particle was equivalent to that in Case 1-3. In Case 1-4, the particle flow structure during the powder filling was different from that in Case 1-1 to Case 1-3. Accordingly, a particular feature of the particle stream such as concave structure was not formed in Case 1-4. At the final state, the resulting pile of Case 1-4 was slightly higher than that of Case 1-1 to Case 1-3. Consequently, the coarse graining DEM was shown to simulate the original particle system in the powder die-filling. Subsequently, air flow was investigated during the powder die-filling. At 0.10 s, circulating air flow was observed at left side in all the cases, though the magnitude of the fluid velocity of Case 1-4 was different from that of Case 1-1 to Case 1-3. At 0.15 and 0.19, circulating air flow and upward air flow were respectively observed at left and right side in Case 1-1 to Case 1-3, whereas different flow patterns were observed in Case 1-4. These results indicated that the coarse graining DEM could reproduce the airflow in the original systems.

Fig. 4 shows typical snapshots of the spatial location of the particles in the shoe region at 0.10 s, 0.15 s, 0.19 s, and the final state. Calculation results of Case 1-1 was addressed at first. The top free surface of the particle in the shoe sloped down to the right wall at 0.10 s because of the particle migration to the die. At 0.15 s, the slope was reduced and a relatively flat surface profile was formed. At 0.19 s, a splash occurred due to the migration of air bubble which was generated in the die. The splash was often observed in the powder die-filling experiments [10,39,40]. At the final state, the remaining particle bed near the right side was lower. Subsequently, evaluation of the coarse graining DEM was described in the shoe region. In Case 1-2 and Case 1-3, the macroscopic dynamics of the particles in the shoe region corresponded to that in Case 1-1. The expansion of the particle bed on the right side due to the air bubble could be simulated using the coarse graining DEM. However, the results of Case 1-4 were different from the other cases. In Case 1-4, the air effect was not significant in the shoe region when the simply large particle system was applied. Thus, the applicability of the coarse graining DEM was proved in the powder die-filling.

Quantitative comparison was described in impact velocity, particle mass transfer rate and air pressure drop. Fig. 5 shows the particle velocity distribution when tip of the powder touched the die floor (0.100 s) in Case 1-1 to Case 1-3. The impact velocity of particles was in good agreement in Case 1-1 to Case 1-3, namely, 0.257 m/s in Case 1-1, 0.251 m/s in Case 1-2 and 0.266 m/s in Case 1-3. Thus, the impact velocity of particles in the original system was shown to be reproduced by the coarse graining DEM. Fig. 6 shows transient changes the particle mass transfer rate during powder die-filling. In Case 1-1, the mass transfer rate increased in the early stage until its maximum value at 0.19 s. The mass flow rate suddenly went down at 0.19 s because of preventing the power flow due to the bubble as well as getting smaller the die inlet

16

area. In Case 1-2 and Case 1-3, the similar trend of the mass transfer rate to Case 1-1 was obtained. These results proved that the coarse graining DEM could reproduce the particle flowability in the original particle system. Regarding the calculation result in Case 1-4, the mass transfer rate was higher than that of Case 1-1 to Case 1-3 during the early filling stage, and besides the maximum value of the transfer rate and the achieved time were obviously different from that of Case 1-1 to Case 1-3. From these results, it was proved that the particle transfer rate in the original particle system could be expected by using the coarse graining DEM.

The change in the spatial-averaged air pressure during the die filling process at the three measurement cells is presented in Fig. 7. In all the measurement cells, pressure profile was quite similar. Around 0.05 s and 0.25 s, the pressure values greatly fluctuated in all the cases because small inlet (or small gap) was created between the die and the shoe. When the inlet of the die was small, invasion of the particle and expansion of the gap significantly and sensitively affected pressure during the powder die-filling. Details of the pressure tendency was described in Case 1-1. The pressure was gradually increased at the early stage of the die filling, where the particle inflow dominated more than the air release. At 0.10 s, half of the shoe hole covered the die mouth. The location of the die and the shoe gave balance between particle inflow and the air release. As the shoe moved further, the release of air dominated more than the particle inflow, and hence the air pressure was observed to gradually decrease. Thus the pressure achieved the brad peak at 0.1 s. The most noticeable feature in this plot was the pressure peak at 0.19 s. The sudden increase of pressure was caused by the entrapped air by the particles. When the splash was occurred, the pressure rapidly decreased. In Cases 1-2 and 1-3, the pressure values were observed following the change in pressure in Case 1-1 in quite similar trends. The pressure peak at 0.19 s was reproduced by both Case 1-2 and Case 1-3. While in Case 1-4, the air pressure

tendency was different from the other cases and any peaks were not appeared. Incidentally, high-frequency small-amplitude fluctuations occurred in all the cases since the particle inflow and the air release were made continuously due to the shoe movement in the powder die-filling.

Thus, the coarse graining DEM could reproduce the original particle system. Agreement between the coarse grained particle systems and original particle system meant that modeling and assumption of the coarse graining DEM were reasonable.

4.2. Case 2

In this case, die filling simulations were conducted using the die type-2. Fig. 8 shows the spatial location of particles as well as the air flow vector at 0.11 s, 0.15 s, 0.18 s and the final state in the die region. In Case 2-1 (original particle system), the particle stream was observed to reach the base of the deep section of the die at 0.11 s. At 0.15 s, the particle flow hit the edge of the die step and then cascaded back over the deep section. Concave structures were formed on the left side and the right side of the particle flow. As the shoe continued to move, the particles fed the shallow section of the die at 0.18 s. Some particles in the lower part of the shallow section were found to cascade over the deep section. After the shoe had completely passed the die, the particles were settled inside the die. The resulting pile surface sloped up to the right side. In Case 2-2 (coarse grain ratio of 2.0) and Case 2-3 (coarse grain ratio of 3.0), the flow pattern of particles was quite similar to that obtained in Case 2-1. The similar position of the front of particle stream at 0.11 s indicated that the particle impact velocity in Cases 2-2 and 2-3 corresponded to that in Case 2-1. However, the results of Case 2-4 were different from other cases. In Case 2-4, the particle flow structure was generally wider than that in Case 2-1 to Case

2-3 during the powder die-filling. The final state showed that the resulting pile in Case 2-4 was noticeably higher than that in Case 2-1 to Case 2-3. Consequently, the coarse graining DEM was shown to simulate the particle behavior in the original particle system in die type-2 as well. The good agreement between the original particle system and the coarse grain model system was further shown from the evaluation of air flow during the powder die-filling. In Case 2-1 to Case 2-3, at 0.11 s and 0.15 s, circulating air flow was observed at the left side of the particle flow in the similar velocity magnitude. However, in Case 2-4, the velocity magnitude was different from other cases. It was proved that the coarse graining DEM could simulate the air effect obtained from the original system.

Fig. 9 presents spatial location of particles at 0.11 s, 0.15 s, 0.18 s and the final state in the shoe region. In Case 2-1, at 0.11 s, the particles top free surface slightly sloped down to the right side due to the particle discharge. The slope was reduced as the shoe moved further and the top surface became relatively flat at 0.15 s. At 0.18 s, a particle splash occurred on the right side due to the moving up bubble from the die. At the final state, a downward slope to the right side was formed due to the inertia effect. Evaluation of the applicability of the coarse graining DEM was made in the same manner as previously. The macroscopic dynamic of the particles top free surface, including the splash in Case 2-2 and Case 2-3 corresponded to that in Case 2-1. Whereas in Case 2-4, the results were noticeably different from the other cases. During the powder die-filling process, bed height in Case 2-4 was noticeably lower than that in the other cases. Additionally, the splash did not occur in Case 2-4. These results indicated that the effect of air on the original particles in the shoe region was reproducible by the coarse graining DEM.

In the same way as Case 1, quantitative comparison was described in impact velocity, particle mass transfer rate and air pressure drop. Fig. 10 shows the impact velocity of the powder

19

when the particles collided with the die floor (0.116 s) in Case 2-1 to Case 2-3. The impact velocities of particles in Case 2-1, Case 2-2 and Case 2-3 were, respectively, 0.231 m/s, 0.220 m/s and 0.226 m/s. Hence, the impact velocity was shown to be reproduced by the coarse graining DEM. Fig. 11 presents the evolution of the rate of particle mass transfer from the shoe into the die. In Case 2-1, the mass transfer rate in the early stage gradually increased until 0.18 s, and sharply decreased after that. As described in the previous case, the sudden decrease of the mass transfer corresponded to the occurrence of the particle splash in the shoe region. In Case 2-2 and Case 2-3, the transient changes of the mass transfer rate corresponded to that in Case 2-1. These results indicated the particle flowability in the original system was reproducible by the coarse graining DEM. Whereas in Case 2-4, the peak of mass transfer appeared earlier than the other cases. After reaching its maximum value, the change of the mass transfer gradually decreased over time. Consequently, the effectiveness of the coarse graining DEM was proved in predicting the particle transfer rate in the original system. Fig. 12 shows the air pressure change at the three measurement cells during the powder die-filling process. In all the measurement cells, pressure profile was quite similar. Around 0.05 s and 0.25 s, fluctuations appeared in all cases because of the same reasons of Case 1. In Case 2-1 to Case 2-3, the pressure gradually increased from around 0.05 s to 0.10 s, and gradually decreased after that. As mentioned in section 4.1, the increase and decrease of the pressure value were influenced by the entering particles and the escaping air, respectively. The most significant feature was the sudden increase in pressure due to the entrapped air around 0.18 s. The pressure value immediately decreased once the air bubble released from the die. And then, the pressure gradually decreased as the die filling proceeded further. However, in Case 2-4, the pressure values were different from the other

cases. The pressure of Case 2-4 was generally lower than Case 2-1 to Case 2-3. Besides, such a pressure peak was not found in the simply large particle system.

Thus, the coarse graining DEM could reproduce the original particle system because modeling and assumption of the coarse graining DEM were reasonable.

5. Conclusions

In the present study, applicability of the integrated DEM-CFD method was examined in a powder die-filling process. Specifically, the coarse grain model was evaluated by comparing the macroscopic characteristics of the gas-solid flows between the original system and the coarse grain model system. We found that the particle flow behavior in the original particle system was suitably reproduced by the coarse grain model system, based on the qualitative and quantitative comparison. From the qualitative comparison, the particle macroscopic flow pattern in coarse grain model system corresponded to that in the original particle system. In addition, the particle splash inside the shoe, which regarded as a critical air effect during die filling, was successfully demonstrated in both the original particle system and the coarse grain model system. From the quantitative comparison, the mass transfer rate and transient change of air pressure in the die region between the original particle system and the coarse grain model system were in an excellent agreement. It was verified that the coarse graining DEM was adequate to predict the flowability of particles in the original particle system. Accordingly, applicability of the Integrated DEM-CFD method was proved in the powder die-filling processes, and the coarse graining DEM could predict the original particle behavior as well as the air flow.

Acknowledgements

References

[1]   C. Hildebrandt, S.R. Gopireddy, A.K. Fritsch, T. Profitlich, R. Scherließ, N.A. Urbanetz, Evaluation and prediction of powder flowability in pharmaceutical tableting, Pharm. Dev. Technol. 24 (2019) 35–47. https://doi.org/10.1080/10837450.2017.1412462.

[2]   Y. Guo, K.D. Kafui, C.Y. Wu, C. Thornton, A Coupled DEM/CFD Analysis of the Effect of Air on Powder Flow During Die Filling, AIChE J. 55 (2009) 49–62.

[3]   Y. Guo, C.Y. Wu, K.D. Kafui, C. Thornton, 3D DEM/CFD analysis of size-induced segregation during die filling, Powder Technol. 206 (2011) 177–188. https://doi.org/10.1016/j.powtec.2010.05.029.

[4]   E.N. Nwose, C. Pei, C.Y. Wu, Modelling die filling with charged particles using DEM/CFD, Particuology. 10 (2012) 229–235. https://doi.org/10.1016/j.partic.2011.11.010.

[5]   I.C. Sinka, L.C.R. Schneider, A.C.F. Cocks, Measurement of the flow properties of powders with special reference to die fill, Int. J. Pharm. 280 (2004) 27–38. https://doi.org/10.1016/j.ijpharm.2004.04.021.

[6]   H. Yao, Y. Mori, K. Takabatake, X. Sun, M. Sakai, Numerical investigation on the influence of air flow in a die filling process, J. Taiwan Inst. Chem. Eng. 90 (2018) 9–17. https://doi.org/10.1016/j.jtice.2017.11.031.

[7]   C.Y. Wu, DEM simulations of die filling during pharmaceutical tabletting, Particuology. 6 (2008) 412–418. https://doi.org/10.1016/j.partic.2008.07.008.

[8]   Y. Guo, C.Y. Wu, K.D. Kafui, C. Thornton, Numerical analysis of density-induced

segregation during die filling, Powder Technol. 197 (2009) 111–119.

[9]   L.A. Mills, I.C. Sinka, Effect of particle size and density on the die fill of powders, Eur. J.

        Pharm. Biopharm. 84 (2013) 642–652. https://doi.org/10.1016/j.ejpb.2013.01.012.

[10]   C.Y. Wu, L. Dihoru, A.C.F. Cocks, The flow of powder into simple and stepped dies,

        Powder Technol. 134 (2003) 24–39. https://doi.org/10.1016/S0032-5910(03)00130-X.

[11]   Y. Tsuji, T. Kawaguchi, T. Tanaka, Discrete particle simulation of two-dimensional

        fluidized bed, Powder Technol. 77 (1993) 79–87. https://doi.org/10.1016/0032-
        5910(93)85010-7.

[12]   S. Wang, K. Luo, C. Hu, J. Lin, J. Fan, CFD-DEM simulation of heat transfer in fluidized

        beds: Model verification, validation, and application, Chem. Eng. Sci. 197 (2019) 280–

        295. https://doi.org/10.1016/j.ces.2018.12.031.

[13]   Z. Jiang, T. Hagemeier, A. Bück, E. Tsotsas, Color-PTV measurement and CFD-DEM

        simulation of the dynamics of poly-disperse particle systems in a pseudo-2D fluidized

        bed, Chem. Eng. Sci. 179 (2018) 115–132. https://doi.org/10.1016/j.ces.2018.01.013.

[14]   S. Kuang, M. Zhou, A. Yu, CFD-DEM modelling and simulation of pneumatic conveying:

        A review, Powder Technol. 365 (2019) 186–207.

        https://doi.org/10.1016/j.powtec.2019.02.011.

[15]   M. Zhou, S. Wang, S. Kuang, K. Luo, J. Fan, A. Yu, CFD-DEM modelling of hydraulic

        conveying of solid particles in a vertical pipe, Powder Technol. 354 (2019) 893–905.

        https://doi.org/10.1016/j.powtec.2019.07.015.

[16]   Y. Shigeto, M. Sakai, Arbitrary-shaped wall boundary modeling based on signed distance

functions for granular flow simulations, Chem. Eng. J. 231 (2013) 464–476.

https://doi.org/10.1016/j.cej.2013.07.073.

[17] X. Sun, M. Sakai, Immersed boundary method with artificial density in pressure equation

for modeling flows confined by wall boundaries, J. Chem. Eng. Japan. 50 (2017) 161–

169. https://doi.org/10.1252/jcej.16we115.

[18] X. Sun, M. Sakai, Numerical simulation of two-phase flows in complex geometries by

using the volume-of-fluid/immersed-boundary method, Chem. Eng. Sci. 139 (2016) 221–

240. https://doi.org/10.1016/j.ces.2015.09.031.

[19] X. Sun, M. Sakai, Direct numerical simulation of gas-solid-liquid flows with capillary

effects: An application to liquid bridge forces between spherical particles, Phys. Rev. E.

94 (2016) 063301. https://doi.org/10.1103/PhysRevE.94.063301.

[20] H. Udono, K. Uruga, T. Tsukada, M. Sakai, Numerical study on rheological properties for

dispersed and aggregated particle systems, Powder Technol. 361 (2020) 203–209.

https://doi.org/10.1016/j.powtec.2019.09.041.

[21] H. Udono, M. Sakai, A numerical study on dynamic inertial focusing of microparticles in

a confined flow, Granul. Matter. 19 (2017) 79. https://doi.org/10.1007/s10035-017-0758-

x.

[22] Y. Mori, C.-Y. Wu, M. Sakai, Validation study on a scaling law model of the DEM in

industrial gas-solid flows, Powder Technol. 343 (2019) 101–112.

https://doi.org/10.1016/j.powtec.2018.11.015.

[23] M. Sakai, M. Abe, Y. Shigeto, S. Mizutani, H. Takahashi, A. Viré, J.R. Percival, J. Xiang,

C.C. Pain, Verification and validation of a coarse grain model of the DEM in a bubbling fluidized bed, Chem. Eng. J. 244 (2014) 33–43. https://doi.org/10.1016/j.cej.2014.01.029.

[24] M. Sakai, Y. Yamada, Y. Shigeto, K. Shibata, V.M. Kawasaki, S. Koshizuka, Large-scale discrete element modeling in a fluidized bed, Int. J. Numer. Methods Fluids. 64 (2010) 1319–1335.

[25] M. Sakai, S. Koshizuka, Large-scale discrete element modeling in pneumatic conveying, Chem. Eng. Sci. 64 (2009) 533–539. https://doi.org/10.1016/j.ces.2008.10.003.

[26] K. Takabatake, Y. Mori, J.G. Khinast, M. Sakai, Numerical investigation of a coarse-grain discrete element method in solid mixing in a spouted bed, Chem. Eng. J. 346 (2018) 416–426. https://doi.org/10.1016/j.cej.2018.04.015.

[27] Z. Xie, Y. Shen, K. Takabatake, A. Yamaguchi, M. Sakai, Coarse-grained DEM study of solids sedimentation in water, Powder Technol. 361 (2019) 21–32. https://doi.org/10.1016/j.powtec.2019.11.034.

[28] P.A. Cundall, O.D.L. Strack, A discrete numerical model for granular assemblies, Geotechnique. 29 (1979) 47–65. https://doi.org/10.1680/geot.1979.29.1.47.

[29] S. Ergun, Fluid flow through packed columns, Chem. Eng. Prog. 48 (1952) 89–94.

[30] C.Y. Wen, Y.H. Yu, A generalized method for predicting the minimum fluidization velocity, AIChE J. 12 (1966) 610–612. https://doi.org/10.1002/aic.690120343.

[31] T.B. Anderson, R. Jackson, Fluid mechanical description of fluidized beds: Stability of the State of Uniform Fluidization, Ind. Eng. Chem. Fundam. 7 (1968) 12–21. https://doi.org/10.1021/i160025a003.

[32] G. Basinskas, M. Sakai, Numerical study of the mixing efficiency of a batch mixer using the discrete element method, Powder Technol. 301 (2016) 815–829. https://doi.org/10.1016/j.powtec.2016.07.017.

[33] G. Basinskas, M. Sakai, Numerical study of the mixing efficiency of a ribbon mixer using the discrete element method, Powder Technol. 287 (2016) 380–394. https://doi.org/10.1016/j.powtec.2015.10.017.

[34] M. Sakai, T. Kazuya, T. Kotaro, K. Hatano, A. Minakuchi, Why do wet-particles adhere to a high- speed roll in a three-roll mill ?, Phys. Fluids. 31 (2019) 1–15. https://doi.org/10.1063/1.5085693.

[35] M. Sakai, How should the discrete element method be applied in industrial systems?: A review, KONA Powder Part. J. 2016 (2016) 169–178. https://doi.org/10.14356/kona.2016023.

[36] M. Sakai, Y. Shigeto, G. Basinskas, A. Hosokawa, M. Fuji, Discrete element simulation for the evaluation of solid mixing in an industrial blender, Chem. Eng. J. 279 (2015) 821–839. https://doi.org/10.1016/j.cej.2015.04.130.

[37] M. Sakai, Y. Mori, X. Sun, K. Takabatake, Recent Progress on Mesh-free Particle Methods for Simulations of Multi-phase Flows: A Review, KONA Powder Part. J. (2019) 1–13. https://doi.org/10.14356/kona.2020017.

[38] T. Kajishima, S. Takiguchi, H. Hamasaki, Y. Miyake, Turbulence structure of particle-laden flow in a vertical plane channel due to vortex shedding, JSME Int. J. Ser. B. 44 (2001) 526–535. https://doi.org/10.1299/jsmeb.44.526.

[39] L.C.R. Schneider, A.C.F. Cocks, A. Apostolopoulos, Comparison of filling behaviour of metallic, ceramic, hardmetal and magnetic powders, Powder Metall. 48 (2005) 77–84. https://doi.org/10.1179/003258905X37549.

[40] C.Y. Wu, A.C.F. Cocks, Numerical and experimental investigations of the flow of powder into a confined space, Mech. Mater. 38 (2006) 304–324. https://doi.org/10.1016/j.mechmat.2005.08.001.

Table 1. Physical properties

Item	Value
Solid phase	
Particle density (kg/m^3)	1.5×10^3
Spring constant (N/m)	50
Coefficient of friction	0.30
Coefficient of restitution	0.90
Gas phase	
Gas viscosity (Pa.s)	1.8×10^{-5}
Gas density (kg/m^3)	1.0

Table 2. Simulation conditions

	Computational particle size (μm)	Coarse ratio	Particle system	Particle number	Die type
Case 1-1	125	1.0	Original	540,000	
Case 1-2	250	2.0	Coarse-grained	67,500	
Case 1-3	375	3.0	Coarse-grained	20,000	1
Case 1-4	375	1.0	Simply large	20,000	
Case 2-1	125	1.0	Original	540,000	
Case 2-2	250	2.0	Coarse-grained	67,500	
Case 2-3	375	3.0	Coarse-grained	20,000	2
Case 2-4	375	1.0	Simply large	20,000	
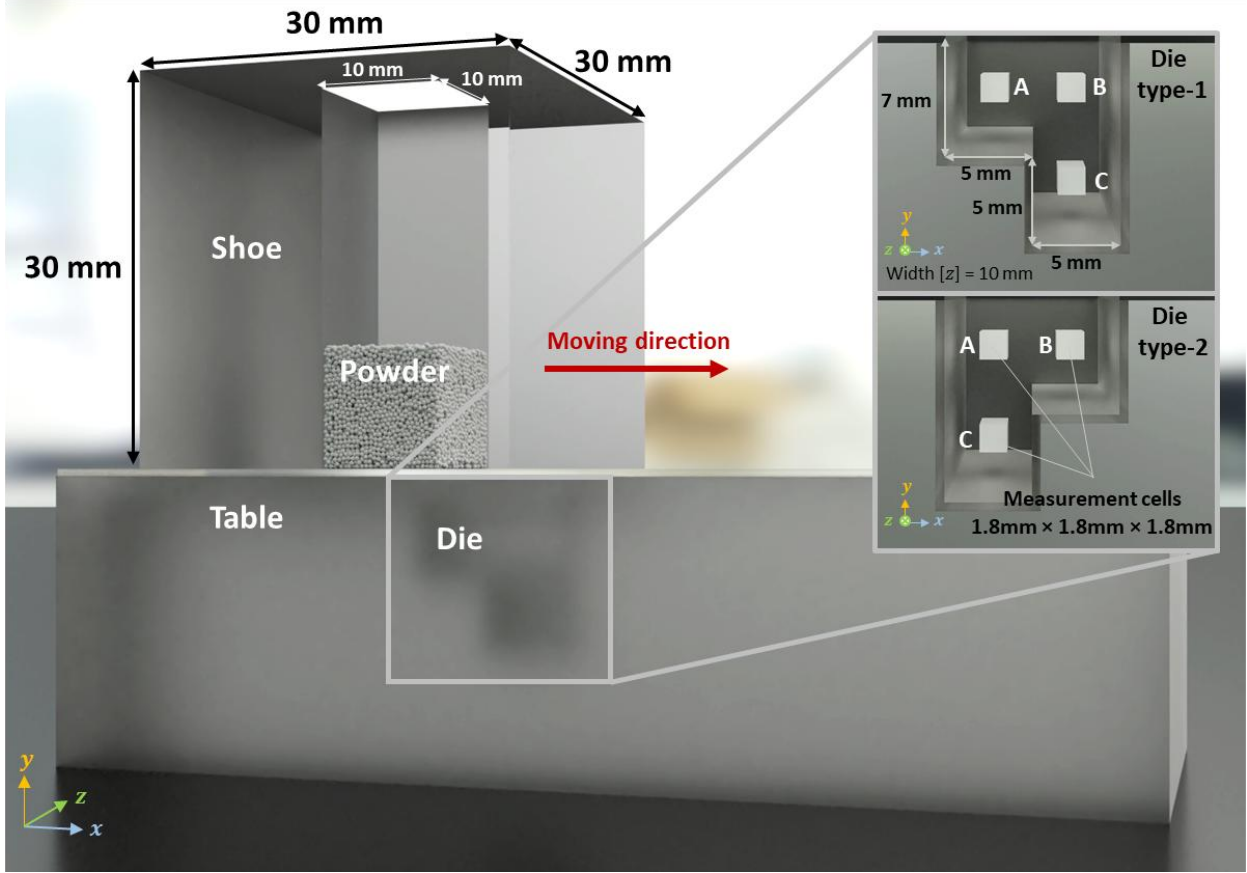
Fig. 1. Geometry of the die filling system including two types of die and the measurement cells.

(a)   SDF
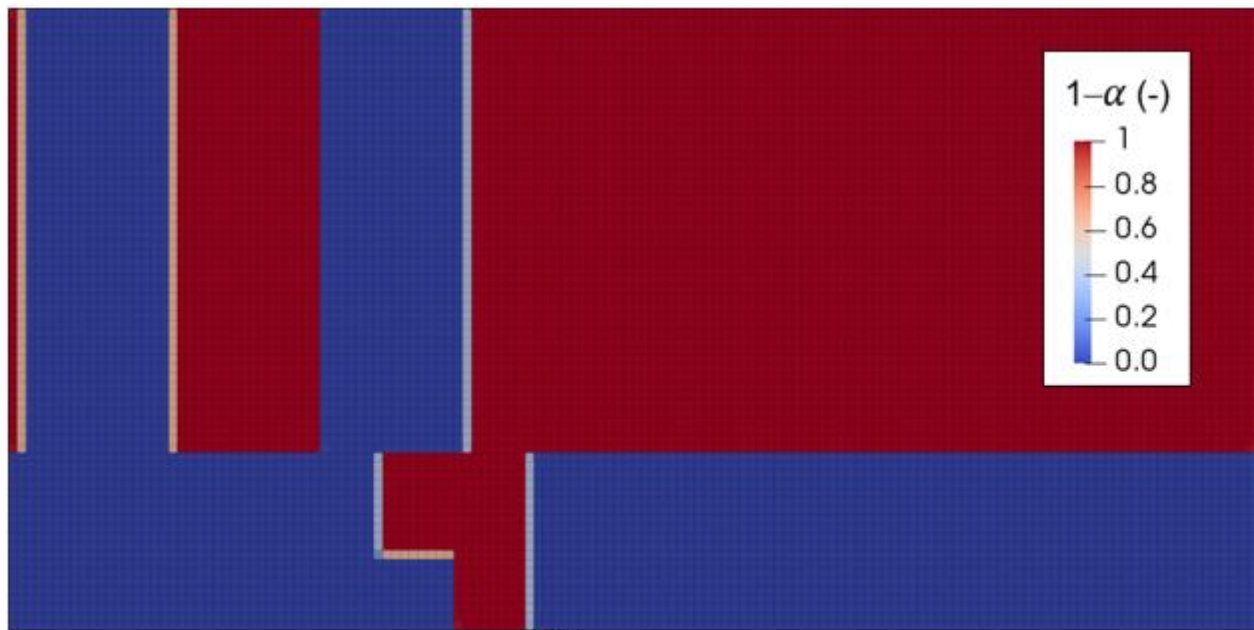
(b)   IBM

Fig. 2. The vertical cross-section view of the SDF and the IBM in the die filling device with die type-1.

Velocity (m/s)

0.10 s

0.15 s

0.19 s

Final state

Case 1-1　　Case 1-2　　Case 1-3　　Case 1-4
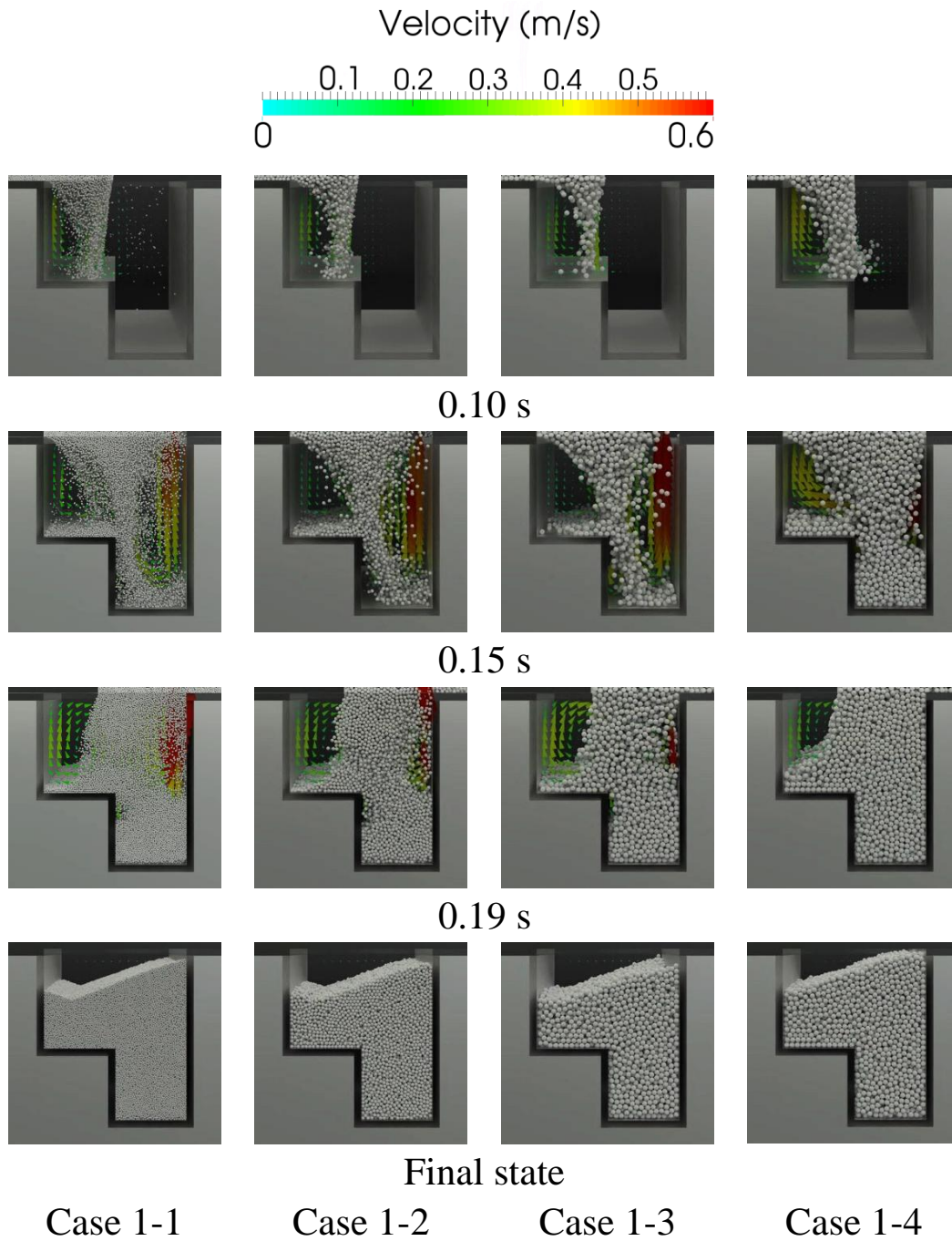
Fig. 3. Particle spatial location and air flow vector in the die region in Case 1.

0.10 s

0.15 s

0.19 s

Final state

Case 1-1   Case 1-2   Case 1-3   Case 1-4
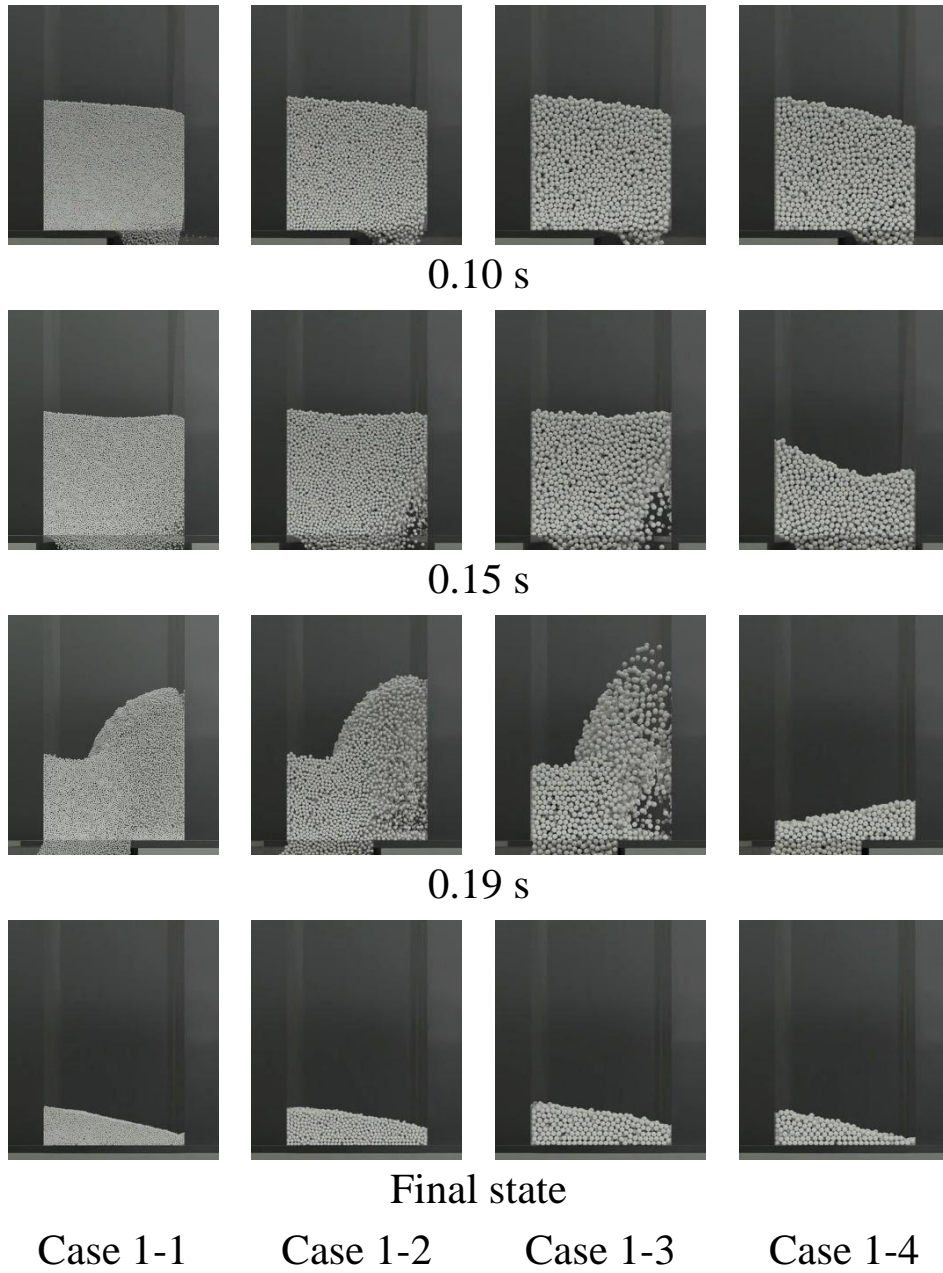
Fig. 4. Particle spatial location in the shoe region in Case 1.
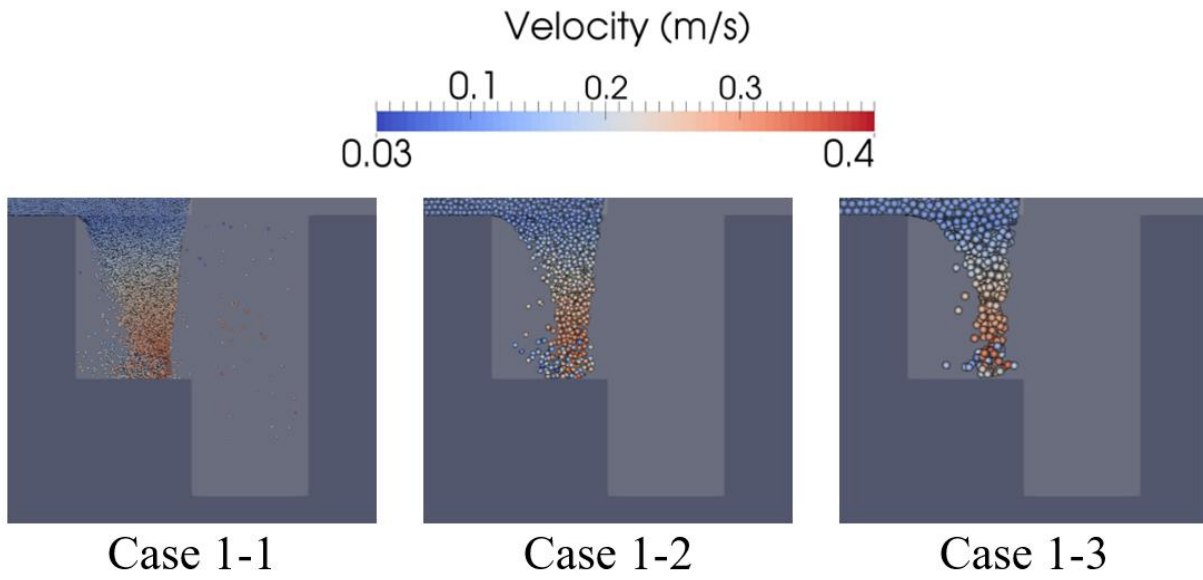
Fig. 5. Particle velocity distribution at 0.100 s for Case 1-1, Case 1-2 and Case 1-3.
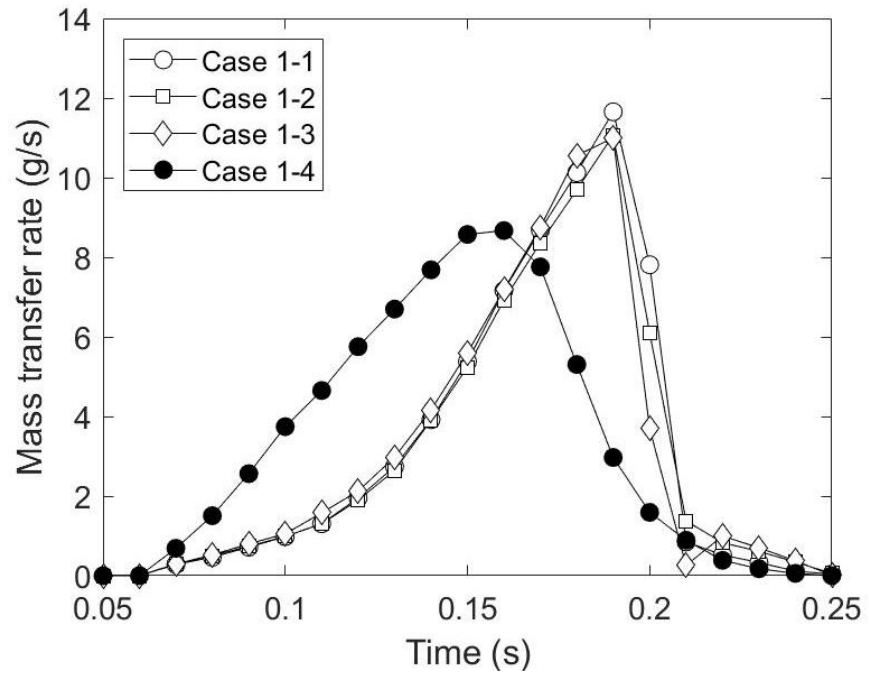
Fig. 6. Time evolution of particle mass transfer rate in Case 1.
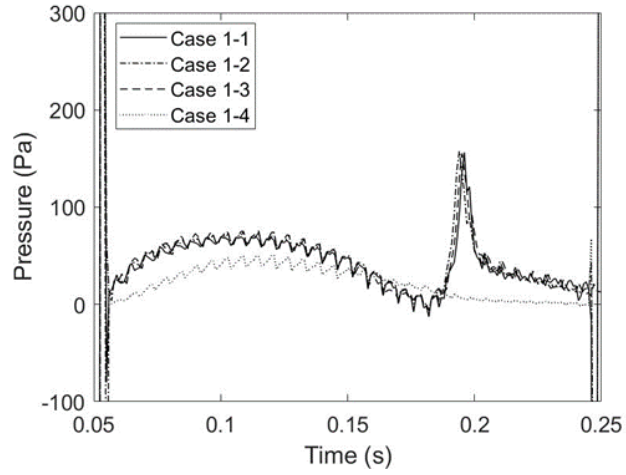
(a) Cell A
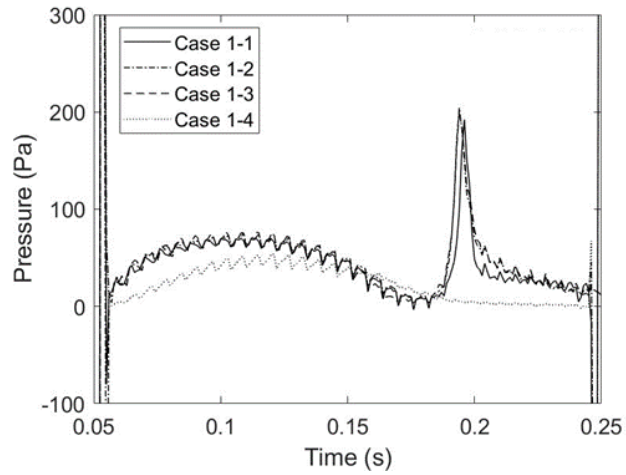
(b) Cell B
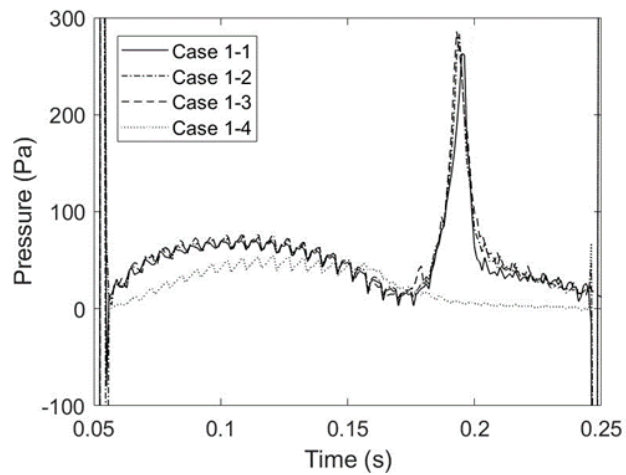
(c) Cell C

Fig. 7. Transient change of pressure measured at cell A, cell B and cell C in Case 1
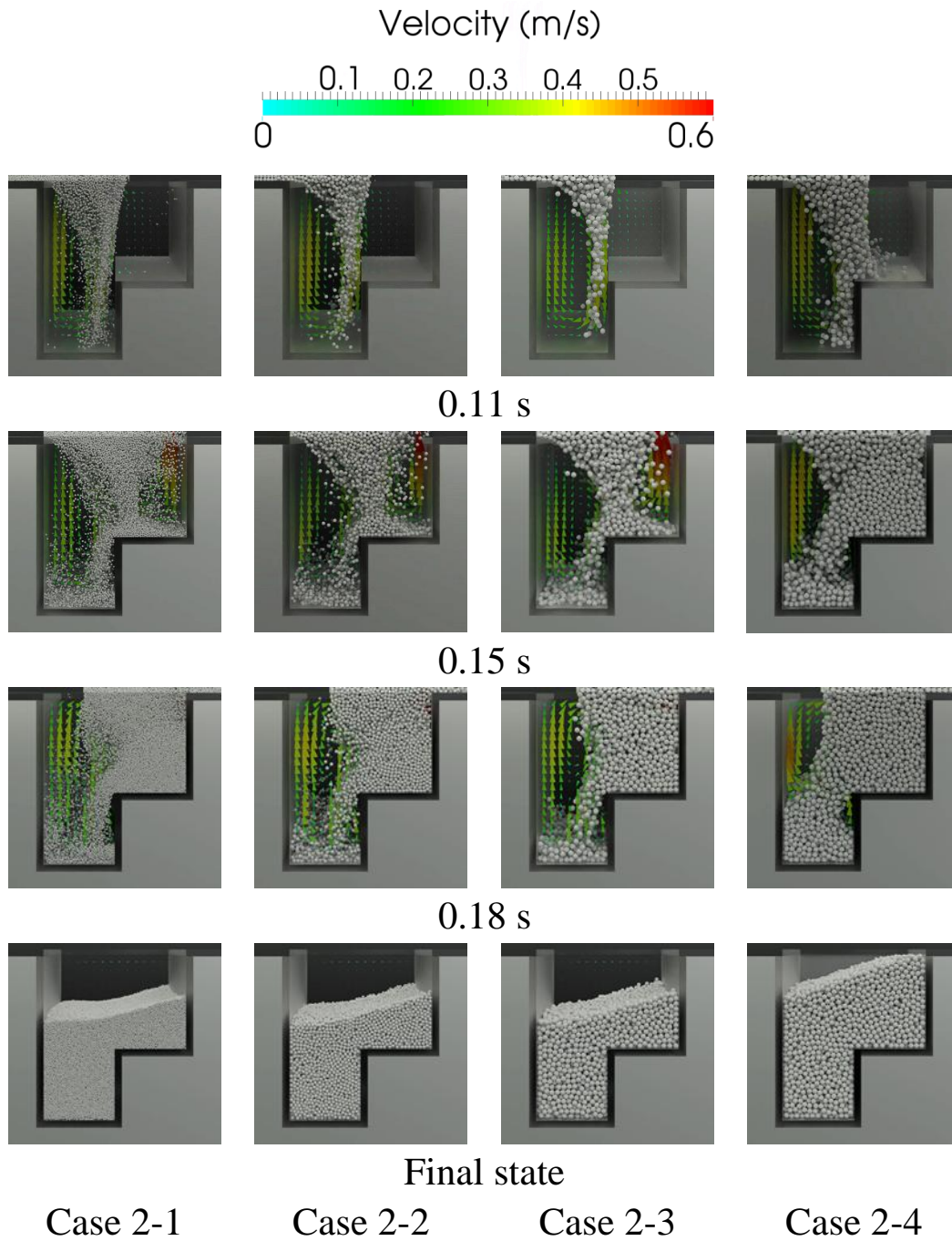
Fig. 8. Particle spatial location in the die region in Case 2.

0.11 s

0.15 s

0.18 s

Final state

Case 2-1   Case 2-2   Case 2-3   Case 2-4
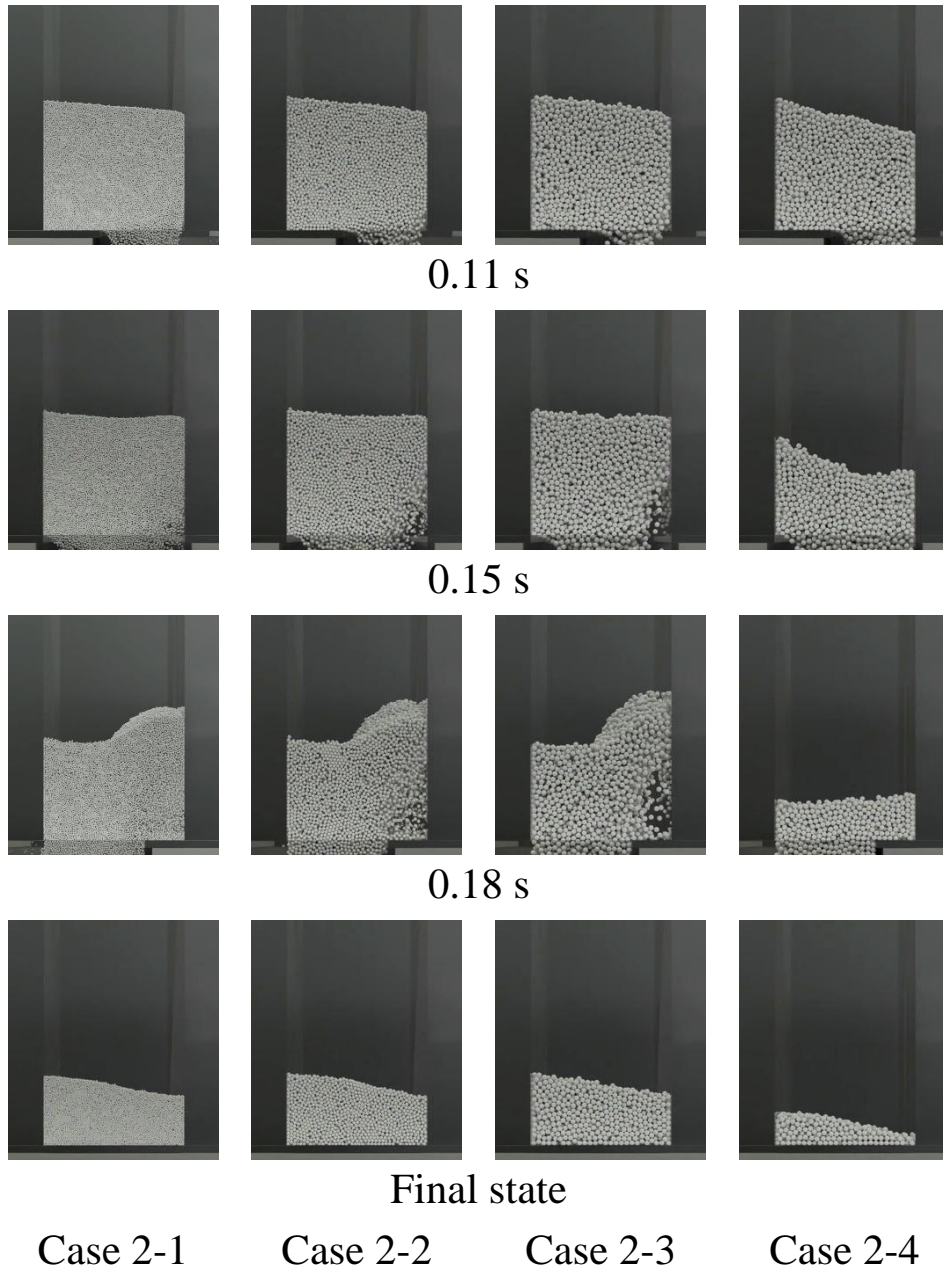
Fig. 9. Particle spatial location in the shoe region in Case 2.
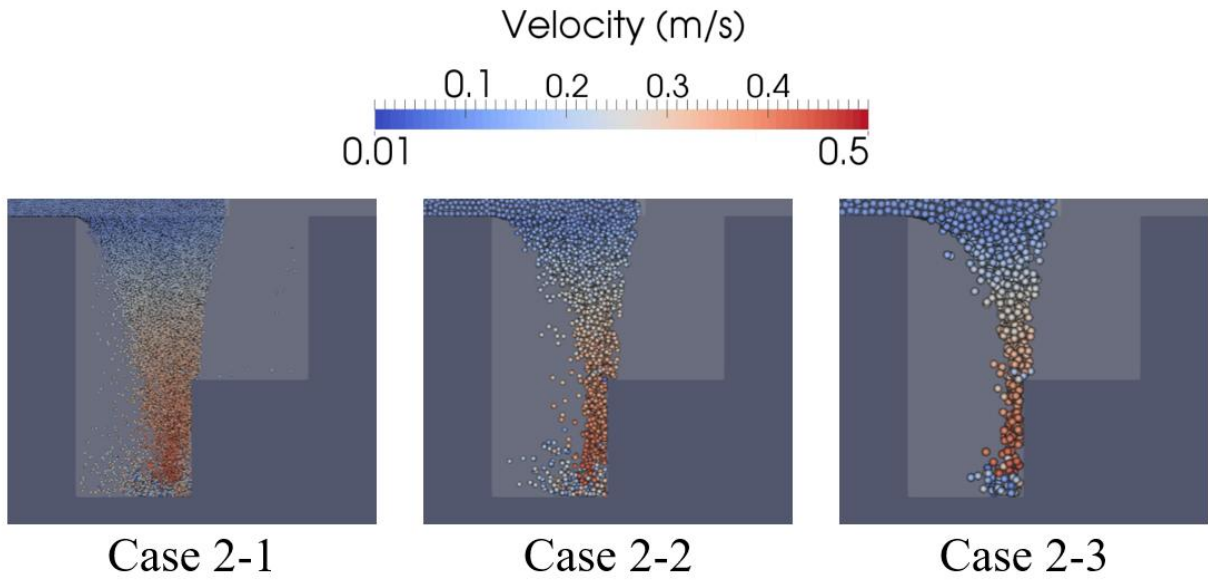
Fig. 10. Particle velocity distribution at 0.116 s for Case 2-1, Case 2-2 and Case 2-3.
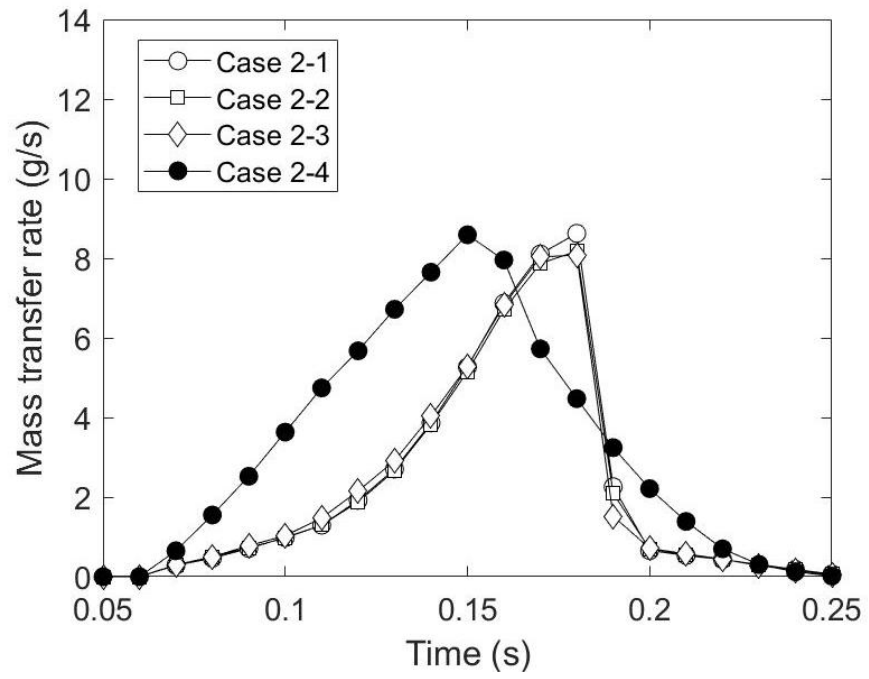
Fig. 11. Time evolution of particle mass transfer rate in Case 2.
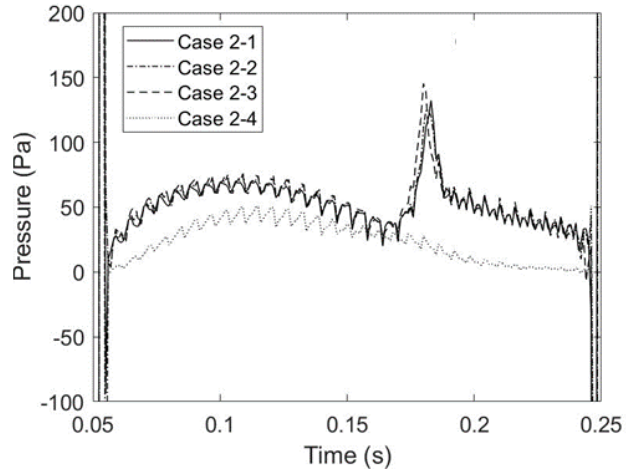
(a) Cell A
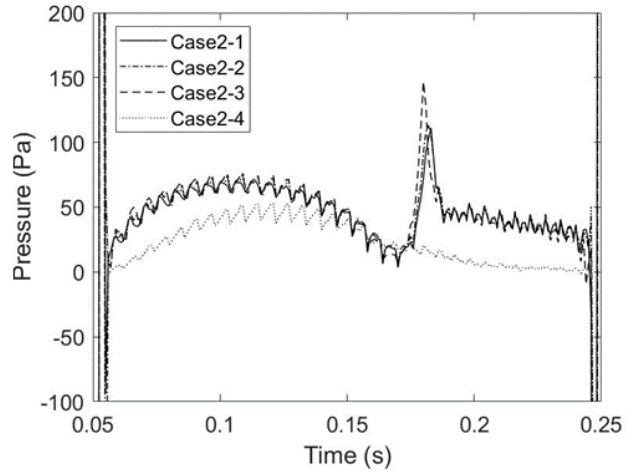
(b) Cell B
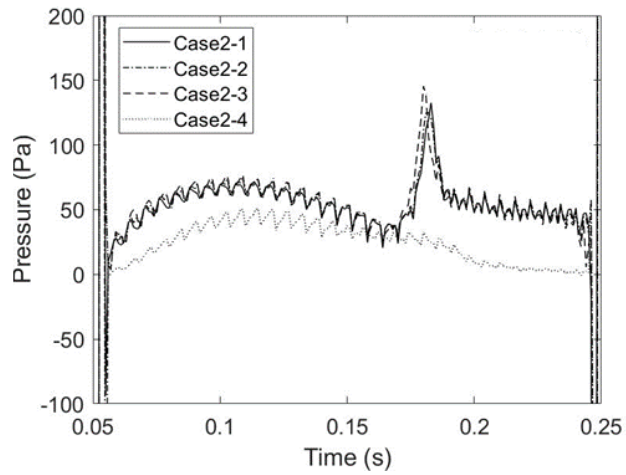
(c) Cell C

Fig. 12. Transient change of pressure measured at cell A, cell B and cell C in Case 2.